Left and Right-Handed Light Reflection and Emission in Ultrathin Cellulose Nanocrystals Films with Printed Helicity

Daria Bukharina[1], Lindsay Southard[1], Botyo Dimitrov[1], Justin A. Brackenridge[1], Saewon Kang[2], Peng Min[1], Yanan Wang[3], Dhriti Nepal[5], Michael E. McConney[5], Timothy J Bunning[5], Nicholas A. Kotov[3,4], Vladimir V. Tsukruk[1]*

[1] *School of Materials Science and Engineering, Georgia Institute of Technology, Atlanta, GA, USA*

[2] *Thin Film Materials Research Center, Korea Research Institute of Chemical Technology, Daejeon, Korea*

[3]*Department of Chemical Engineering, University of Michigan, Ann Arbor, MI, USA*

[4] *Department of Materials Science and Engineering, University of Michigan, Ann Arbor, MI, USA*

[5] *Air Force Research Laboratory, Wright-Patterson Air Force Base, Dayton, Ohio 45433, USA*

ABSTRACT

Natural polymers, plant-derived nanocelluloses in particular, self-organize into hierarchical structures, enabling mechanical robustness, bright iridescent color and emission, and polarized light reflection. These biophotonic properties can be facilitated by the assembly of individual components upon evaporation, such as cellulose nanocrystals (CNCs), which exhibit a left-handed helical pitch morphology of a chiral nematic type. As a novel step, this work demonstrates how optically active films with pre-programmed different handedness (left or right) can be constructed via shear-induced twisted printing with layered clockwise and counter-clockwise shearing vectors. The resulting large-area thin films are transparent yet exhibit pre-determined mirror symmetrical optical activity enabling distinction of absorbed and emitted circularly polarized light with different pre-programmed handedness. This processing method allows for sequential printing of thin and ultrathin films with twisted layered organization and inverted on-demand helicity. The resulting thin films possess complex light polarization behavior due to step-like changes in linear birefringence within each deposited layer and give rise to circular birefringence, not seen in conventional natural films as revealed with Muller matrix analysis. Furthermore, intercalating an achiral organic dye into the printed structures induces circularly polarized luminescence while preserving high transmittance and controlled handedness. These results suggest that twisted sequential printing can facilitate the construction of chiroptical metamaterials with tunable circular polarization, absorption, and emission for optical filters, photonic coatings, chiral sensors, and optical encryption.

Keywords*: biophotonic cellulose nanocrystals, helicity inversion, handedness on-demand, multifunctional photonic composites, circularly polarized luminescence.*

* *Corresponding author:* E-mail: vladimir@mse.gatech.edu

1. INTRODUCTION

In nature, the appearance of diverse colors can be caused by the presence of pigments, texturing, or structural organization. The latter, specifically, causes the appearance of structural colors through periodic organization, and is due to the combination of light diffraction, interference, scattering, and absorption in complex photonic crystals. This spectacular natural phenomena can be seen in plants[1], peacocks[2], chameleons[3], butterflies[4], and beetles.[5] Moreover, natural photonic materials often reconcile important multifunctional properties, such as high strength and toughness combined with bright iridescence such as in the case of the Jewel Beetle.[5,6,7,8] These bio-based robust photonic materials are promising candidates for light manipulation and harvesting applications under extreme conditions.[6,7,8]

Bioderived polymers such as cellulose, chitin, and chitosan are of particular interest for functional applications due to their abundant availability, sustainability, and great mechanical performance.[9,10,11] Among these examples, nanocelluloses are by far the most studied candidates for next generation structural and photonic materials with great photonic and mechanical integrity. Cellulose materials can be broken down into isolated needle-like nanostructures, cellulose nanocrystals (CNCs) with high aspect ratios (reaching 50-100), low density and high strength, and can exhibit diverse surface chemistry. In concentrated suspensions CNCs undergo a spontaneous transition into a lyotropic chiral nematic liquid crystalline phase with natural left-handed helicity.[12,13] This helicoidal structure with a pitch length of several hundred nanometers can further be preserved during slow drying, resulting in a thin film with selective circularly polarized light discrimination due to Bragg reflection and bright iridescent colors.[13,14] As observed, spontaneous evaporation-induced assembly exclusively yields the nature-preferred left-handed helical organization due to intrinsic topographical features of the nanocrystals including twisted shapes and skewed cross sections, in addition to the amphiphilic nature of the nanocrystal facets.[15,16]

The CNCs organization in the lyotropic liquid crystalline phase and within thin films upon slow water evaporation is controlled by the nanocrystals' microenvironment, including surface charge[17], solution ionic strength[18], and pH[19], as well as the dimensions, aspect ratio, and surface chemistry, all affecting their chiral nematic organization and pitch length. Furthermore, field-directed CNC assembly and their organization has been studied under magnetic-field alignment[20,23], electric-field alignment[21], and mechanical shear alignment.[24] Overall, the application of external fields leads to preferred tactoids orientation or uniaxial orientation as controlled by the field direction and strength.[22]

Achieving both high orientation order and macroscopic control of the twist direction is desired for optically graded materials with low optical losses narrow bandgaps. This control allows for the manipulation of the handedness of circularly polarized light, resulting in enhanced iridescence and broader chiroptical properties.[23,24,25] Moreover, for advanced photonic applications, handedness switching is desirable yet rarely achieved in natural and synthetic materials.[26,27] For instance, the development of bio-derived robust, flexible materials for chiroptical sensing, optical communication, optical encryption and optical coding require controllable and diverse chiroptical structures with tunable pitch length and handedness, in contrast to the naturally spontaneous self-assembly process.[28] Conversely, pre-programmed chiral assemblies have been achieved by stacking achiral objects using inorganic nanomaterials. For example, Probst et al., have shown gold nanoparticles assembled into dimer chains inside nanochannels.[29] By stacking those microarrays at different angles, the CD signal can be modulated, and mirrored. Hu et al., showed how grazing incidence spraying of plasmonic 1D nanowires, can be assembled into chiral Bouligand structures.[30] The Langmuir-Schaefer deposition allowed for inorganic nanowires to be deposited by sequential dipping enabling diverse chiroptical photonic crystals.[31,32]

Additionally, development of nanoscale chiral emissive materials has been critical over the past decade. These materials can manipulate light at the nanoscale, enabling the development of advanced photonic devices, including ultra-compact optical components and high-resolution imaging systems.[33,34] In this context, cellulose nanocrystals found their way to be applied when integrated with optically active components such as organic dyes[35], quantum dots[36], or nanorods.[37,38] Although, the $|g_{lum}|$ in some cases was as high as 0.4 [36,38,37], the limitation of such host-guest co-assembly remains in exclusive single-handedness and thus, fixed circularly polarized luminescence (CPL). Advanced optical applications require switchable handedness.

Here, we demonstrate unique optical bio-films with multilayered twisted morphology with on-demand different handedness (right or left). These thin helical twisted films can be sequentially printed from a polymer-mediated, shear-induced assembly of uniformly and highly aligned cellulose nanocrystals in a clockwise and counterclockwise manner with pre-programmed twisting angle value and sign (**Fig. 1**). Both *left*- or *right*- handed transmittance and emission modes have been demonstrated. The resulting chiroptical properties of these transparent yet optically active ultrathin films are controlled by rotation of linear birefringence within individually printed layers with twisted organization. Furthermore, this sequential printing can be further scalable, is conducted in ambient conditions from aqueous suspensions in relatively fast pace (hours instead

of days), and can be further optimized for different bio-derived materials and substrates for various printed bioderived photonic metamaterials.

2. RESULTS AND DISCUSSION

2.1 Cellulose nanocrystal-polyelectrolyte thin films printing.

Cellulose nanocrystal films with printed twisted multi-layers were fabricated by sequential shear deposition of individual nano-scale layers at a pre-programmed rotating angle using doctor-blade coating approach (**Fig. 1**).[39]

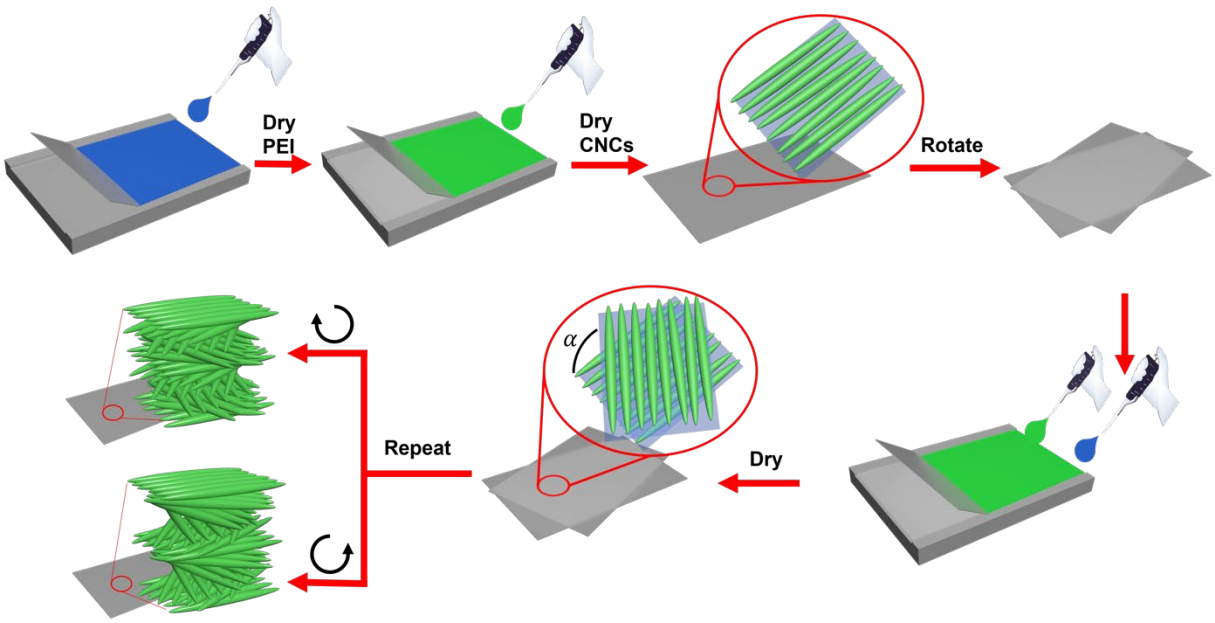

Figure 1. Schematic of the sequential shear printing of helical photonic structures with pre-determined twisting angle and orientational direction.

First, an ultra-thin nanostructured layer (of around 100-200 nm, analyzed below) of CNCs was shear-coated onto a quartz slide resulting in uniaxial alignment of the nanocrystals on the substrate and their orientational order analyzed (see below). Then, a second layer was deposited on top with the direction of printing rotated by a selected angle with respect to the alignment direction of the first layer by rotating the substrate. This approach provides previously inaccessible combination of simplicity of practical realization with complexity of three-dimensional helical structure of the cellulose composites. Left- (clockwise (CW)) or right-(counterclockwise (CCW)) handed multilayered twisted organization can be constructed in this manner, depending

on the rotation direction (**Fig. 1**). Although, the resulting structures are not classical morphologies as observed in self-assembled CNC films, due to controlled twisting of the deposited layers, the resulting films exhibit “discrete” helical organization composed of anisotropic nanoscale “blocks” able of efficient light polarization as pre-programmed by the fabrication design.

The suspension concentration and the deposition speed are the two determinant factors for the deposition of a uniform layer of controlled thickness.[40] In order to control these factors, CNC suspensions of different concentrations were deposited at different shearing conditions, with their orientational ordering evaluated with atomic force microscopy (AFM) (see **Fig. S1-S5**).[43] Overall, a 5wt.% CNC suspension showed the best alignment utilizing optimal shearing condition (speed of 3 mm/s) with a 100 μm gap between the blade and the substrate. Thus, these conditions were selected for further studies. A cationic achiral polyethylenimine (PEI) nanoscale layer was introduced as a mediating layer in order to balance the overall Columbic interactions and stabilize the printed multilayered films (**Fig. S6**).[41] The PEI interlayer promotes absorption of negatively charged CNCs and minimizes non uniformity, helping to reduce light scattering in the final structure and improve optical activity. Thus, each discrete layer fabricated in this manner is a combination of the sequentially deposited CNCs and PEI layers, unless otherwise specified.

Detailed orientational analysis was conducted for each deposited layer to establish preferential orientation angle and azimuthal distribution of nanocrystal axes from high-resolution AFM images with pixel resolution reaching 2 nm. From these data, the orientational order parameter, *S,* calculated from azimuthal distribution reached very high values: 0.84 for larger areas that include some defects and tactoids boundaries (**Fig. S2**), and reached very high values of 0.96 for local orientation after negation of microscopic defects (**Fig. S4, S5**).

Considering that the natural twisting angle between individual nanocrystal monolayers is ~ $8-10°$,[42] we selected $10°$ as the lowest twisting angle to explore here. The upper limit for twisting angle was chosen as $30°$ to assure consistent correlation between twisted layers and desired orientation direction. The morphology of printed films was thoroughly characterized with high-resolution AFM imaging for different sheared layers with changing orientation (**Figs. 2 a-h, S2-S5**). First, the mean roughness (R_q) of the deposited layers as measured from AFM images was within 2 to 3 nm within 1 x 1 μm area indicating a very smooth surface with low contribution to light scattering. The large-scale 2D orientational order parameter calculated from the azimuthal distribution of nanocrystal orientation reached 0.84 for the different layers deposited at 0-, 60- and 90^o orientation angles (**Fig. S2,S3**).[43] With $S = 0$ corresponding to isotropic randomness and $S = 1$ corresponding to perfect alignment, the degree of organization is on par or substantially higher

than other cases of nanofiber-based coatings and regular chiral nematic phases.[44,43] This value exceeds natural orientation order for these lyotropic chiral nematic phases (0.6-0.8) and indicates very high shear-enhanced orientation.[24]

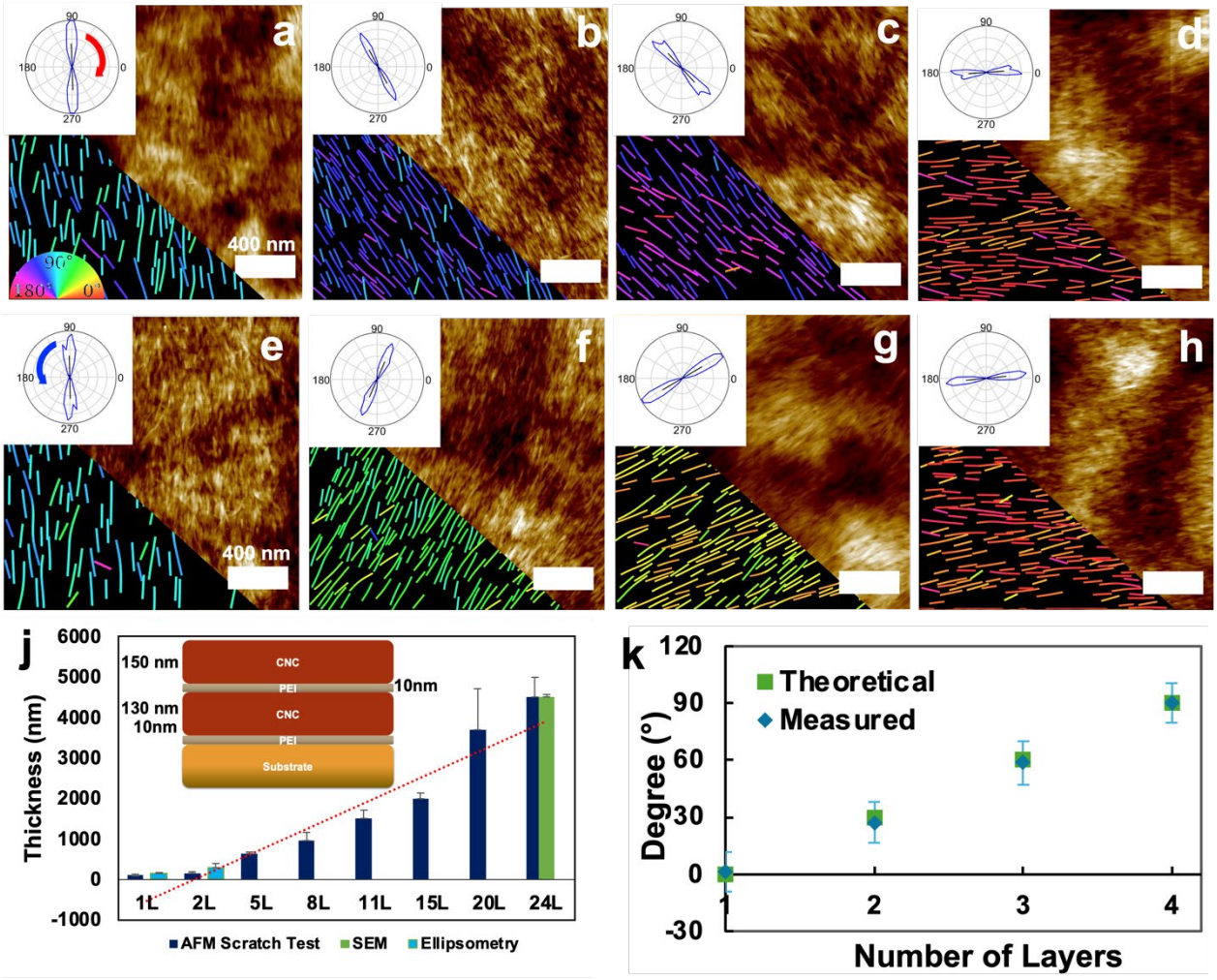

Figure 2. High-resolution AFM topography images of the CNC layers color-coded according to their orientation shear-deposited (a, e) along the shearing direction, (b,f) with substrate rotated 30°, (c,g) 60°, and (d,h) rotated 90°. Insets are azimuthal distributions obtained from image analysis, the black line in the middle indicates the nanocrystals' mean orientation. Red and blue arrows in images *a* and *e* show the substrate rotation direction. (j) Total films thickness as a function of number of printed layers. The red dotted line indicates linear regression, the inset schematic shows the sequence of the deposited layers with individual thicknesses. (k) The theoretical twisting angle between layers as set during printing process and measured twisting angle from the azimuthal orientational distribution as a function of number of layers, the error bars are obtained from the analysis of at least 10 images.

To demonstrate how different directions of the substrate rotation results in left or right orientation of the NCs, we show images in **Fig 2a-d** and **e-h** color-coded according to the CNCs orientation

obtained from AFM topography images of subsequentially printed layers. We can see nanocrystals perfectly mirrored on AFM images and opposite colors on their color-coded insets for each next layer analyzed, confirming control of their deposition during the process (more details in **Fig. S4, S5**). The local alignment of CNCs was even higher, reaching S_{2D}=0.96 for each layer studied with higher resolution for smaller areas with increased spatial resolution (**Fig. S5**). Thus, precisely programmed orientation of cellulose nanocrystals on the local and global scale within each deposited layer was achieved for all printing directions and at all sequentially deposited layers.

The film thickness was further monitored with ellipsometry, AFM and SEM and compared to the theoretically expected thickness calculated using the individual layer thickness times the number of layers (see Supporting Information). As measured with ellipsometry, the thickness of the PEI layer was ~ 10 nm, while the thickness of the deposited CNCs layer was close to 150 nm for total about 160 nm per composite layer. As the thickness increased and approached the ellipsometry limit, thicker films were further measured using AFM scratch tests (**Table S1, Fig. S6**).[45] Overall, the thickness of the films increased linearly with the number of deposited layers, indicating layer-by-layer printing consistency across 24-36 deposition steps (**Fig. 2j**).

The thicknesses obtained from ellipsometry, AFM scratch test, and the overall thickness measured via cross-sectional SEM for thicker films were all in good agreement (**Fig. 2j**). The overall thickness of the films as measured by cross-sectional SEM varied from 4.5 to 6 μm for 24-layered samples deposited at 30° rotation (**Fig. S8**). SEM images–showed a characteristic periodic layered morphology with traditional Bouligand organization (**Fig. 3b,c**), similar to conventional self-assembled CNC films, confirming the presence of helicoidal organization within the printed films (**Fig.S7, S8**).[18]

Notably, high-resolution cross sectional SEM images were collected for 24L samples deposited at 30° rotation to further confirm helical organization (**Fig. 3b,c**). Images revealed twisted periodic layers within printed films, and showed their twisting in opposite directions. The average increment in film growth was close to 150 nm/layer that is consistent with thickness of individual layers measured independently (**Fig. S8**). Based on those measurements, theoretical pitch length ($P=\frac{360^\circ}{rotation\ angle} * thickness\ of\ each\ layer$)[31] was estimated to be around 1800 nm (for samples deposited at 30°) and 5400 nm for 10°. Corresponding NIR light absorption signals couldn't be successfully measured due to only 1-2 full pitches printed that is not enough for sufficient structural color appearance (see Supporting Information). Thus, overall, unique thin films

fabricated here were completely transparent in the visible range but showed activ chiroptical properties as detailed below.

2.2 Chiroptical properties.

Overall, printed films did not exhibit iridescent coloration, appeared uniform and transparent with high light transmittance varying from 90 to 86% in the 250 to 800 nm range, and showed intense optical anisotropy and circular dichroism (CD signal) (**Figs. 3a, S9, S10**).

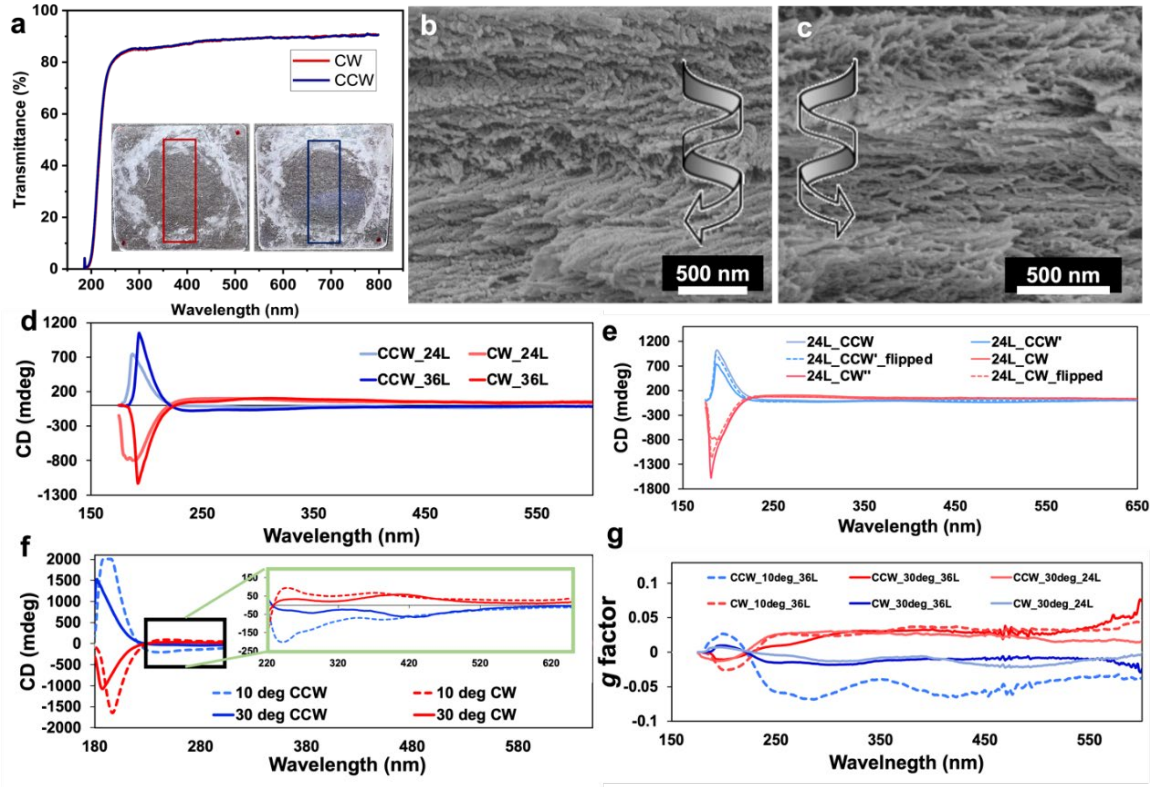

Figure 3. (a) Transmittance UV-vis spectra of the 24L samples deposited at 30° twisting angle. Insets are digital photographs of samples deposited on quartz (2.5 x 2.5 cm), red and blue boxes indicate the measured regions. (b) SEM image of the cross-section of CCW 24L sample deposited at 30° and (c) SEM image of the cross-section of CW 24L sample deposited at 30°. Arrows are digitally inserted to demonstrate twisting of the layers within the films. (d) CD spectra of 24 and 36 layers clockwise (CW) and counterclockwise (CCW) chiral films deposited at 30°. (e) CD spectra obtained from 24L samples deposited at 30°, in direct and flipped positions. (f) CD spectra of the CW and CCW films deposited at different angles, 10 and 30°. Films contain 36 and 24 layers, respectively. (d) *g-factor* calculated for different rotation angles and number of layers.

Samples fabricated at 30 and 10° demonstrated the most variability in their chiroptical properties and were studied in detail. The reflectance of linearly polarized light of these engineered printed films was anisotropic as observed under crossed polarizers. For films deposited at a 30° rotation

angle, we observed a change in color appearance with the change of angle (induced light polarization). The color intensity also increased with increased number of deposited layers (**Fig. S9**). CD spectroscopy showed a dramatic transformation in optical activity of films depending upon specific printing conditions (**Fig. 3d-g)**. Specifically, CD spectra for samples deposited at 10 and 30° rotations possess a complex shape with intense positive or negative CD peaks for different twisted printing conditions **(Fig. 3d,f).**

The CD spectra displayed several peaks including one near 200 nm and lower intensity broad peaks near 250 nm and 420 nm (**Fig. 3d**). This is in contrast to a single broad positive peak around 400 nm observed in traditionally assembled drop-cast CNCs films (**Fig.S7).**[12,14,18] It is also noted that the CD spectra obtained for CW and CCW samples with opposite sign of twisting angle are symmetrical, indicating construction of the CNCs films of mirror handedness (**Fig. 3d**). For the films deposited at a 10° rotation, we observed the peaks to consistently red-shift due to increase of pitch length compared to larger twisting angle (**Fig. 3f**). [46] To independently confirm that CD spectra are not dominated by linear dichroism or linear birefringence (see figure 4 for detailed analysis of the components), we further measured the films' CD spectra at regular and flipped positions (beam passes through substrate and then the film *vs* film and then substrate for all previous measurements).[47] Importantly, the CD signal signs and positions were consistent (**Fig. 2e**, **S11**).

Next, to evaluate the strength of chiral signal that is a thickness-independent characteristic parameter, we calculated the asymmetry factor, also known as *g-factor*, from ellipticity (θ) according to eq. 1: [48]

$$g = \frac{\Delta A}{A} = \frac{\theta(mdeg)}{32980 * A} \qquad (1)$$

This dimensionless criterion quantifies chiroptical strength of a material and allows for a quantitative comparison with others in the context of broadly used CD metric. The *g factor* values increased with the number of deposited layers (**Fig. 3g**). The *g factor* reached maximum values of $g = -0.07$ at λ=280, 411 nm for 10° samples and $g = \pm 0.03$ at λ=265, 408 nm, for the 30° samples (**Fig. 3d**). These values of *g-factors* are two orders of magnitude higher than those of conventional organic chiral molecules ($|g| \sim 10^{-4}$-10^{-3}) and are comparable to CNCs films obtained at slow evaporation ($|g| \sim 10^{-1}$) indicating that sequential printing does not compromise overall optical activity.[49,50,51,52]

Previously reported in literature, shear-deposited CNCs films demonstrated transparent anisotropic organization but did not have helical ordering, and thus no the structural color.[22,39] In the case of our thin films high transparency did not lead to loss of chiroptical activity due to intrinsic helicity of CNC layers stacked. Printing of twisted structures as Bragg stacks (at 90°) also led to photonic bandgap but complete lack of chiroptical activity.[53] Additionally, printed multilayered films are stable over months and even under high humidity in contrast to traditional self-assembled CNCs films (**Figs. S12, S13**).[54,55]

The origin of optical activity in our printed films (the three distinct peaks) was examined using a combination of spectroscopic ellipsometry and FTDT calculations.[30,56] Obtained films are expected to have high linear anisotropy, and thus, the chiroptical properties can be influenced by linear and circular dichroism, and linear and circular birefringence.

First, we turned to Mueller Matrix (MM) analysis in order to evaluate different optical components (see detail in Supporting information).[57] For non-depolarizing samples (**Fig. S14**), the Mueller matrix can be related to circular dichroism and birefringence, ***CD and CB***, as well as the horizontal and 45° projections of linear dichroism (***LD and LD'***) and linear birefringence (***LB and LB'***) as:

$$M = exp\begin{pmatrix} A & -LD & -LD' & CD \\ -LD & A & CB & LB' \\ -LD' & -CB & A & -LB \\ CD & -LB' & LB & A \end{pmatrix} \quad (2)$$

Where, $m_{11,22,33,44}$=A, $m_{12,21}$= -LD, $m_{13,31}$=-LD', $m_{14,41}$=CD, m_{23}=CB, m_{24}=LB', m_{32}=-CB, m_{34}=-LB, m_{42}=-LB', m_{43}=LB. Circular birefringence (CB) indicates the difference in speed of propagation of left- and right-handed circular polarization states, whereas the CD measures a sample's selectivity for transmission of left- and right-handed circular polarization.

From this analysis, we observed that in contrast with measured-on-spectropolarimeter CD, the m_{14} element corresponding to circular dichroism is close to zero at wavelengths above 250 nm (**Fig. 4**, CD panels). Moreover, the LD and LD' components are of the same order of magnitude and are negligible compared to the LB and LB' optical components with highest contribution coming from the bottom-right nine elements of the Mueller Matrix (eq. 2). When diagonal elements (m_{22}, m_{33}) are equal to 1, the polarization states of light will not be changed upon passing through the samples, whereas at -1, light's polarization states will be converted to their orthogonal counterparts (left to right and vice versa). Analysis of the diagonal elements (m_{22}, m_{33}) (**Fig. S15, S16**) indicates a value of 1 in the wavelength range from 400 to 900 nm. At lower wavelengths,

m_{22} and m_{33} both rapidly decrease, approaching -1 around 200 nm. Compared to the CD spectra in Figure 3, the CD peaks switch sign at the same wavelengths, the behavior typical for optical retarders.[58]

This analysis indicates that these films act as linear optical retarders, as retardance appears in the bottom-right nine elements of the Mueller Matrix with dominant contribution from both circular and linear birefringence and not common CD contribution. Circular birefringence peak can be observed around 250 nm (**Fig.4**, CB panels) for samples deposited at 30° and red shifting to 290 nm for 10° samples. This shift and peak position corresponds well to those observed on CD spectra (**Fig. 3 d,f**), indicating that this peak is indeed originated from circular birefringence. The peaks around 420 nm are less prominent compared to other peaks but correspond to the observed linear birefringence activity as well.

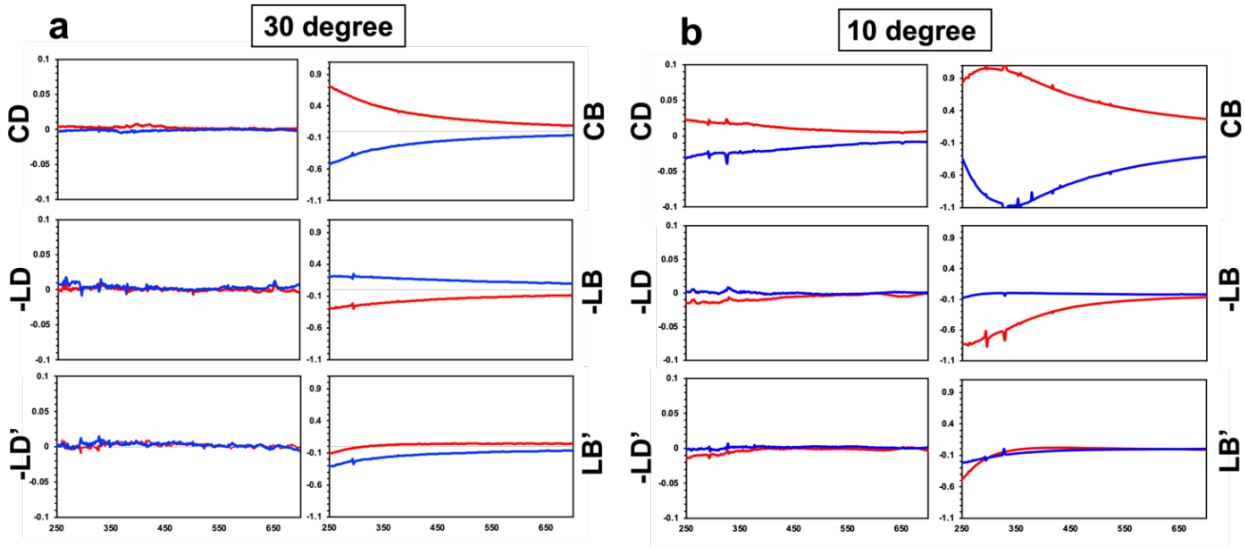

Figure 4. Key elements of the measured Mueller Matrices obtained for samples deposited at (a) 30° rotation angle and (b) 10°. Red lines are for clockwise samples, blue lines are for counterclockwise twisting.

The origin of optical properties was further analyzed with FDTD simulations of optical bandgaps and anisotropies (details in supporting information).[59] First, we analyzed the optical anisotropy of individual layers using spectroscopic ellipsometry and interpreted the results with a biaxial refractive index model (**Fig. S18**). These measurements reveal high local birefringence, with refractive index along the CNC orientation reaching 1.59, and Δn ranging from 0.06 to 0.07 across the whole UV-vis range (**Fig. S18**).

Next, optical response of a pair of optical anisotropic layers stacked at θ =10 and 30° were simulated (**Fig. 5**). CD signal is simulated by passing circularly polarized light through this series of paired optical elements and compared to the experimental results. The CD spectra for rotated layers showed peaks at 205 nm for layers rotated at 30° (**Fig. 5c**), and at 210 nm for 10° (**Fig. 5f**). The appearance of these peaks correspond well to the measured CD spectra (**Fig. 5 b,e**) and confirms their origin is a result of the circular polarization arising at the layers' interface due to the presence of the chiral twisted interface and interactions of twisted anisotropic layers.

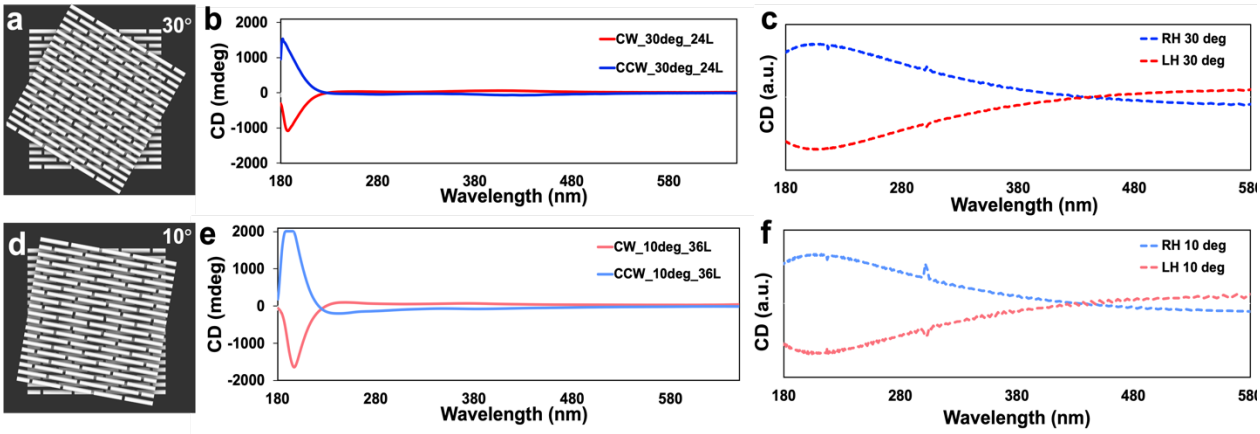

Figure 5. Simulation with model nanocrystals layers rotated (a) 30° and (d) 10°, (b) and (e) measured by CD spectroscopy and (c) and (f) simulated CD spectra for 30 and 10° samples, respectively. Spectra (b) and (e) obtained from the same samples as those in figure 3f.

2.3 Printed twisted films with circularly polarized emission.

Furthermore, the ability of generating circularly polarized luminescence (CPL) was explored in these printed films by adding emitting component into the starting polymeric mixture. Thus, a known achiral organic dye, Rhodamine 6G (R6G) with an emission peak around 550 nm was added within each PEI layer (**Fig. S21**).[60] The resulting films appeared transparent with a light transmittance around 80% in the whole visible range (**Fig. S22**).

When observed under UV light (254 nm), the films exhibited bright green fluorescence (**Fig. 6a inset, S23**). CD spectra exhibited a mirror-symmetric shape, and featured an additional peak around 540 nm, corresponding to the dye emission peak (**Fig. 6, S23**). The CPL spectra revealed symmetrical peaks in the same wavelength region (**Fig. 6c**) for films of opposite handednesses. CPL peaks consistently redshifted in samples deposited at 30, 20, and 10° twisted angles (**Fig. 6c**). The CPL peak is a result of propagation of the light emitted by achiral fluorescent dye through the twisted structure of printed CNC films fabricated here. Thus, an inversion of handedness of

light polarization in printed films discussed above facilitates an inversion of dye-induced light emission polarization. The symmetrical peaks in CPL spectra, coupled with the consistent redshift observed across samples printed at different rotation angles, demonstrate a controlled and predictable manipulation of internally originated circularly polarized emission.

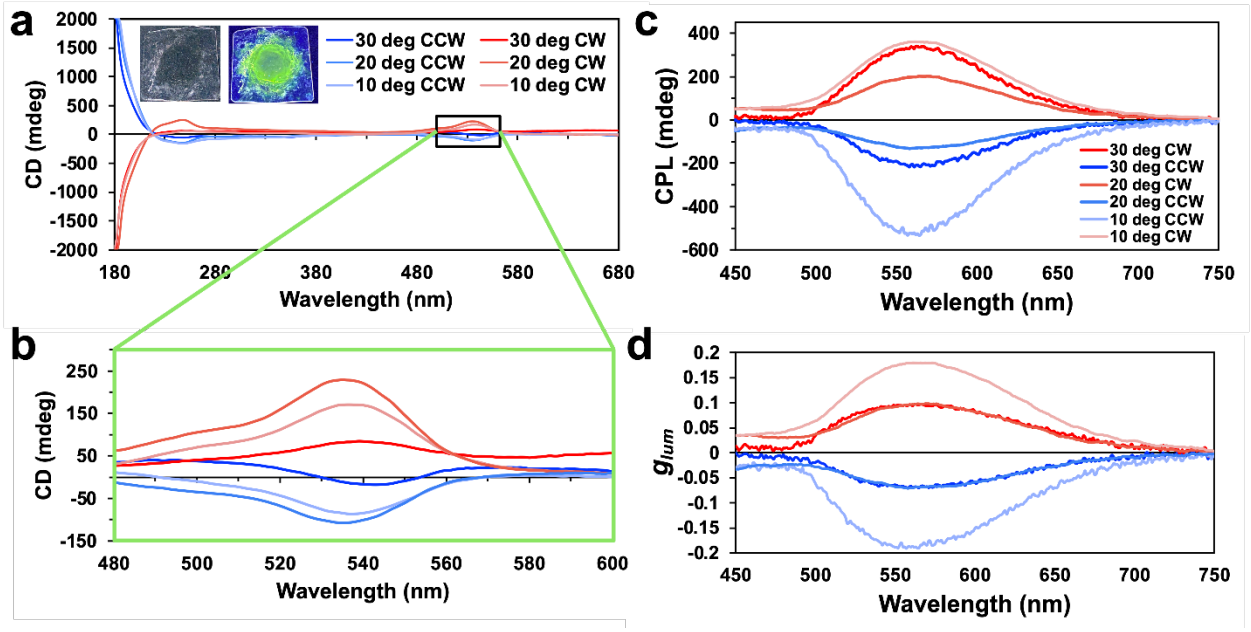

Figure 6. (a) CD spectra of the fluorescent samples printed at different rotation angles, inserts are digital photographs of the samples in visible light and in UV light (254 nm); (b) zoomed-in CD spectra of the same samples (some spectral variations are caused by variability in substrates); (c) CPL spectra and (d) calculated from them g_{lum} of the samples deposited at different rotation angles.

The luminescence asymmetry factor (g_{lum}) calculated from these spectra ranged from ± 0.05 to ± 0.16 at λ=560 nm (**Fig. 6d**). These numbers are high in comparison with g_{lum} reported in the literature for self-assembled cellulose-templated structures.[61,62] Although, comparable in magnitude to some reports[63], in the case of our printed films, the g_{lum} can be tuned with respect to the sign (positive or negative), rarely achieved in self-assembled films.[64] This is on par and better, than many chiral fluorescent and phosphorescent molecules exhibiting CPL whose *g*-values are in the range of 10^{-4}–10^{-1}.[63,65] Such high level of CPL asymmetry is attributed to the controlled helical organization within the films that is possible with the twisted printing approach explored in this work.

3. CONCLUSIONS

In conclusion, we have successfully made ultrathin CNCs films as twisted optical metamaterials with pre-programmed handedness by sequential directional printing of helical (twisted) structures.

The 3D printing implemented in this work enables one to control the chiroptical response of the twisted films via tuning of the deposition conditions including rotation angle, rotation direction, and films thickness. Fabricated twisted films with discrete helical morphology possess diverse unique optical activities with controllable CD peak position, sign, and intensity enabled through a combination of circular and linear birefringence. Furthermore, the printing process is translatable for large-scale films deposition conducted in ambient conditions, making it accessible as well as scalable.

Twisted printed films fabricated here show unique and distinct chiroptical activities: they appear transparent in contrast to traditionally thicker iridescent self-assembled CNC films due to a limited number of pitches (2 to 3 in films fabricated here). This unique high transparency creates unusual ability to induce high optical activity such as circular polarization with very high asymmetry factor for both transmitted and emitted light combined with minimum light reflection. Notably high and controlled sign of CPL asymmetry factors and overall unique optical activity originate from pre-programmed helicity and handedness lead to a tailored combination of circular dichroism and circular birefringence of correlated sequential twisting of individual blocks. Future applications for transparent ultrathin chiroptical films from natural polymers with in-printed discrete helicity can include novel photonic-based encryption, sensing, and computing.

4. MATERIALS AND METHODS

Materials.

Initial PEI solution (PEI materials: $M_w \sim 2{,}000$, $Mn \sim 1800$) 50 wt. % in water was purchased from Sigma Aldrich and further diluted to 0.5 wt. %. An aqueous solution of R6G (2mg/mL) was prepared and mixed with 0.5 wt.% PEI in 1:4 volume ratio. Milli-Q water (18.2 MΩ·cm) was used for all experiments.

Synthesis of cellulose nanocrystals.

The CNCs used in this work were isolated from wood pulp by acid hydrolysis according to the established protocol.[66] Briefly, 5 g of dried wood pulp pieces were added to 95 g of 64 wt.% sulfuric acid solution at 45°C and stirred continuously for an hour. To quench hydrolysis, the reaction solution was poured into a glass container of tenfold acid volume Milli-Q water. The suspension was left overnight to phase separate, followed by the bottom layer being decantated and centrifuged for 10 min at 6000 rpm in order to wash the CNCs suspension.

After the washing steps, the supernatant was removed, ultrapure water added, and the CNCs suspension was dialyzed against water until pH was neutral. In order to obtain a homogeneous and well-dispersed suspension, the resulting suspension was centrifuged again at 10,000 rpm and then tip-sonicated at 40% amplitude, 5 s on - 5 s off, for 4 min and 30 sec using a large tip sonicator (Qsonica Q125 with 1/8" diameter probe).

Doctor Blade-assisted film printing.

Twisted thin films were deposited layer-by-layer via doctor blade deposition on a TQC Sheen Automatic Film Applicator Compact. A quartz substrate was placed on the coating stage and taped on both sides with scotch tape. Tape was also used to control the gap between the blade and substrate, and the gap utilized was 100 μm. First, 5uL of 0.5 wt., % solution of the PEI was deposited along the shear direction. The layer was dried with warm air. Next, 5uL of the 5 wt., % CNC solution was deposited in the same direction as the PEI layer. The drying step was repeated, and the bilayer was formed.

The substrate was controllably rotated at a fixed angle (30 to 10°), and the next PEI layer was deposited. After drying, the following CNC layer was deposited. And these steps were repeated until the full rotation was complete or the desired number of layers was deposited. For CPL active films, the same steps were implemented except the intermediate PEI layer was substituted with a R6G-PEI mixture.

Atomic Force Microscopy.

High-resolution *AFM* images were obtained on the Dimension Icon microscope (Bruker) in the tapping mode in air with 1024 x 1024 pixels with ultrasharp AFM tips of radii ~2-5 nm according to usual procedure.[67] Each layer was deposited onto a piranha treated silicon wafer and scanned in at least 5 different locations. Image analysis was conducted with Nanoscope and Gwiddyon. The orientation analysis of AFM images with pixel resolution of 2-5 nm sufficient for resolving individual nanocrystals was performed in GTFiber software.[43]

Electron Microscopy.

SEM images were taken on Hitachi SU-8230 Electron microscope operated at 3kV voltage. Films on substrates were cut with sharp razor blade and attached perpendicularly to the SEM mount. Samples were sputter-coated with gold for 45 sec at 30 mA (3 nm gold layer thickness).

UV-Vis and CD Spectroscopy.

UV-Vis spectroscopy was done using a Shimadzu UV-3600 Plus UV-Vis-NIR Spectrophotometer within a range of 185 to 1000 nm in transmittance mode, as well as in 1000-3000 nm range. CD spectroscopy was done with JASCO- J815 spectropolarimeter.

Mueller Matrix Spectroscopy.

For measuring the single layer thickness, the Woollam M-2000U Spectroscopic Ellipsometer was utilized. The Cauchy model was used to fit PEI layer and CNCs layers. The single-layer CNC film was modelled as an ideal Cauchy dielectric with no extinction coefficient, and with biaxial anisotropy. Model parameter fitting was performed with the VWASE software. Mueller Matrices were obtained in the transmission mode with components normalized with respect to m_{11}.[68]

FDTD calculations.

Ansys Lumerical FDTD (version 2023 R2.1) software was used for simulating the transmittance and circular dichroism spectra. In order to investigate interfacial photonic properties with a manageable computational time, a simplified structure consisting of two layers with a single nanorod thickness and an interlayer spacing was modeled. Each layer contains unidirectionally oriented cylindrical nanorods in a checkerboard configuration. The paired layers are twisted by 10° and 30° mirroring the geometry in respective samples. The geometric parameters are as follows: 15 nm diameter, 15 nm interlayer distance (25 nm between cylinder axes), 10 nm in-layer spacing (20 nm between axes), 10 nm between cylinder bases, and 100 nm length (**Fig. S25**).

The films were then irradiated using left-hand and right-hand circularly polarized light. Transmittance for the different polarizations was then converted to absorbance and used to calculate the circular dichroism as the difference in absorbance multiplied by a constant:

$$\theta(deg) = \Delta A \left(\frac{ln\,10}{4}\right)\left(\frac{180}{\pi}\right) \approx 32.98\,\Delta A \quad (3)$$

Each cylinder was assigned an isotropic dielectric material with a refractive index n=1.65.

Fluorescence Spectroscopy and CPL measurements

Emission spectra were obtained on Shimadzu Fluorospectrophotometer RF-5301PC. Films on quartz slides were attached to the 45-degree stage, while the excitation wavelength was set as 245 nm. The CPL measurements were conducted with JASCO CPL-300, excitation wavelength was chosen to be 280 nm as it demonstrated the highest CPL intensity. Asymmetry factor g_{lum} which is defined as $|g_{lum}| = 2 \times (I_L - I_R)/(I_L + I_R)$[69] , was calculated as $g_{lum} = 2 \times$ [ellipticity/(32980/ln10)]/total florescence intensity.[70]

AKNOWLEDGEMENTS

Financial support for this research was provided by the Air Force Research Laboratory grant FA 8650-22-D5803, Air Force Office for Scientific Research grant FA9550-23-1-0641, and NSF-EPDM project. Facilities at Georgia Tech Institute for Electronics and Nanotechnology supported by the NSF-ECCS-2025462 Award. NAK and YW acknowledge financial support by NSF 2243104, “Center of Complex Particle Systems (COMPASS) and Vannevar Bush DoD Fellowship to NAK ONR N000141812876 and MURI project ONR N00014-20-1-2479. We thank Katherine Cauffiel for valuable discussions.

CONFLICT OF INTEREST

The authors declare no conflict of interest.

TOC

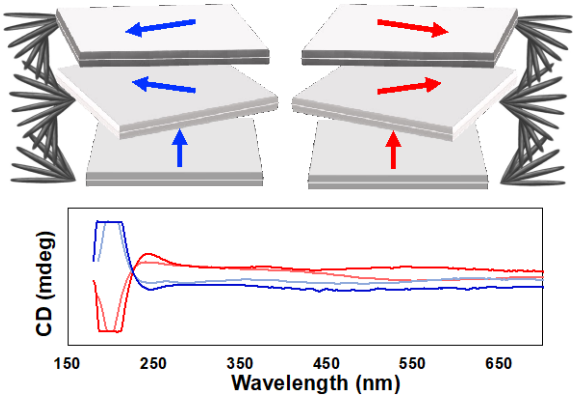

REFERENCES

1 S. Vignolini, E.Moyroud, B. J. Glover, U. Steiner, U. *J R Soc Interface* **2013**, *10* (87), 20130394.

2 J. Zi, X. Yu, Y. Li, X. Hu, C. Xu, X. Wang, X. Liu, R. Fu. *Proc. Natl. Acad. Sci. U.S.A.* **2003**, *100* (22), 12576–12578.

3 J. Teyssier, S. V. Saenko, van der Marel, D.; Milinkovitch, M. C. *Nat. Commun.* **2015**, *6 (1),* 6368.

4 Chen, Y.; Zang, X.; Gu, J.; Zhu, S.; Su, H.; Zhang, D.; Hu, X.; Liu, Q.; Zhang, W.; Liu, D. Zno *J. Mater. Chem.* **2011**, *21 (17)*, 6140.

5 Sharma, V.; Crne, M.; Park, J. O.; Srinivasarao, M. *Science* **2009**, *325* (5939), 449–451.

6 Lawrence, B. D.; Cronin-Golomb, M.; Georgakoudi, I.; Kaplan, D. L.; Omenetto, F. G. *Biomacromolecules* **2008**, *9 (4)*, 1214–1220.

7 Xiong, R.; Grant, A. M.; Ma, R.; Zhang, S.; Tsukruk, V. V. *Mater. Sci. Eng: R.* **2018**, *125*, 1-41.

8 Kato, T.; Uchida, J.; Ichikawa, T.; Sakamoto, T. *Angew. Chem. Int. Ed*. **2018**, *57*, 4355

9 Dumanli, A. G.; Savin, T. *Chem. Soc. Rev.* **2016**, *45*, 6698–6724.

10 S. Venkatarajan, C. Subbu, A. Athijayamani, R. Muthuraja, *Mater. Today: Proc.* **2021**, *47*, 1017.

11 L. Sui, L. Huang, P. Podsiadlo, N. A. Kotov, J. Kieffer, *Macromolecules* **2010**, *43*, 9541.

12 Y. Habibi, L. A. Lucia, O. J. Rojas, *Chem. Rev.* **2010**, *110*, 3479.

13 R. M. Parker, G. Guidetti, C. A. Williams, T. Zhao, A. Narkevicius, S. Vignolini, B. Frka-Petesic, *Adv. Mater.* **2017**, *30*, 1704477.

14 R. J. Moon, A. Martini, J. Nairn, J. Simonsen, J. Youngblood, *Chem. Soc. Rev.* **2011**, *40*, 3941.

15 P.-X. Wang, W. Y. Hamad, M. J. MacLachlan, *Nat. Commun.* **2016**, *7*, 11515.

16 K. W. Klockars, B. L. Tardy, M. Borghei, A. Tripathi, L. G. Greca, O. J. Rojas, *Biomacromolecules* **2018**, *19*, 2931.

17 T. Abitbol, D. Kam, Y. Levi-Kalisman, D. G. Gray, O. Shoseyov, *Langmuir* **2018**, *34*, 3925.

18 D. Bukharina, M. Kim, M. J. Han, V. V. Tsukruk, *Langmuir* **2022**, *38*, 6363.

19 X. M. Dong, D. G. Gray, *Langmuir* **1997**, *13*, 2404.

20 T. Pullawan, A. N. Wilkinson, S. J. Eichhorn, *Biomacromolecules* **2012**, *13*, 2528.

21 B. Frka-Petesic, H. Radavidson, B. Jean, L. Heux, *Adv. Mater.* **2017**, *29*, 1606208.

22 R. A. Chowdhury, S. X. Peng, J. Youngblood, *Cellulose* **2017**, *24*, 1957.

23 X. Zhang, S. Kang, K. Adstedt, M. Kim, R. Xiong, J. Yu, X. Chen, X. Zhao, C. Ye, V. V. Tsukruk, *Nat. Commun.* **2022**, *13*, 5804.

24 R. A. Chowdhury, Md. Nuruddin, C. Clarkson, F. Montes, J. Howarter, J. P. Youngblood, *ACS Appl. Mater. Interfaces.* **2018**, *11*, 1376.

25 M. Kim, K. Pierce, M. Krecker, D. Bukharina, K. Adstedt, D. Nepal, T. Bunning, V. V. Tsukruk, *ACS Nano* **2021**, *15*, 19418.

26 T. Cui, B. Bai, H. Sun, *Adv. Funct. Mater.* **2019**, *29*, 1806692.

27 S. V. Makarov, A. S. Zalogina, M. Tajik, D. A. Zuev, M. V. Rybin, A. A. Kuchmizhak, S. Juodkazis, Y. Kivshar, *Laser Photonics Rev.* **2017**, *11*, 1700108.

28 M. J. Han, M. Kim, V. V. Tsukruk, *ACS Nano* **2022**, *16*, 13684.

29 P. T. Probst, M. Mayer, V. Gupta, A. M. Steiner, Z. Zhou, G. K. Auernhammer, T. A. König, A. Fery, *Nat. Mater.* **2021**, *20*, 1024.

30 H. Hu, S. Sekar, W. Wu, Y. Battie, V. Lemaire, O. Arteaga, L. V. Poulikakos, D. J. Norris, H. Giessen, G. Decher, M. Pauly, *ACS Nano* **2021**, *15*, 13653.

31 J. Lv, D. Ding, X. Yang, K. Hou, X. Miao, D. Wang, B. Kou, L. Huang, Z. Tang, *Angew. Chem. Int. Ed.* **2019**, *131*, 7865.

32 Z. Han, F. Wang, J. Sun, X. Wang, Z. Tang, *Adv. Mater.* **2022**, *35*, 2206141.

33 P. Stachelek, L. MacKenzie, D. Parker, R. Pal, *Nat. Commun.* **2022**, *13*. 553.

34 B. Baguenard, A. Bensalah-Ledoux, L. Guy, F. Riobé, O. Maury, S. Guy, *Nat. Commun.* **2023**, *14*, 1065.

35 J. He, K. Bian, N. Li, G. Piao, *J. Mater. Chem. C* **2019**, *7*, 9278.

36 D. Lu, M. Li, X. Gao, X. Yu, L. Wei, S. Zhu, Y. Xu, *ACS Nano* **2022**, *17*, 461.

37 Y. Shi, Z. Zhou, X. Miao, Y. J. Liu, Q. Fan, K. Wang, D. Luo, X. W. Sun, *J. Mater. Chem. C* **2020**, *8*, 1048.

38 S. Kang, G. M. Biesold, H. Lee, D. Bukharina, Z. Lin, V. V. Tsukruk, Adv. Funct. Mater. 2021, 31, 2104596.

39 S. Shrestha, J. A. Diaz, S. Ghanbari, J. P. Youngblood, *Biomacromolecules* **2017**, *18*, 1482.

40 K. R. Jinkins, J. Wang, J. H. Dwyer, X. Wang, M. S. Arnold, *ACS Appl. Bio Mater.* **2021**, *4*, 7961.

41 G. Decher, M. Eckle, J. Schmitt, B. Struth, *Curr Opin Colloid Interface Sci* **1998**, *3*, 32.

42 K. Adstedt, E. A. Popenov, K. J. Pierce, R. Xiong, R. Geryak, V. Cherpak, D. Nepal, T. J. Bunning, V. V. Tsukruk, *Adv. Funct. Mater.* **2020**, *30*.

43 N. E. Persson, M. A. McBride, M. A. Grover, E. Reichmanis, *Chem. Mater.* **2016**, *29*, 3.

44 R. Blell, X. Lin, T. Lindström, M. Ankerfors, M. Pauly, O. Felix, G. Decher, *ACS Nano* **2016**, *11*, 84.

45 M. Lemieux, D. Usov, S. Minko, M. Stamm, H. Shulha, V. V. Tsukruk, *Macromolecules* **2003**, *36*, 7244.

46 M. Gu, C. Jiang, D. Liu, N. Prempeh, I. I. Smalyukh, *ACS Appl. Mater. Interfaces.* **2016**, *8*, 32565.

47 A. Salij, R. H. Goldsmith, R. Tempelaar, *J. Am. Chem. Soc.* **2021**, *143*, 21519.

48 N. Berova, K. Nakanishi, R. Woody, *Circular Dichroism: Principles and applications*; Wiley-VCH: New York, **2000**.

49 B. R. Baker, R. L. Garrell, *Faraday Discuss.* **2004**, *126*, 209.

50 W. Zhang, X. Cheng, S. H. Chen, M. Anthamatten, *Langmuir* **2023**, *39*, 9180.

51 W. Ma, L. Xu, A. F. de Moura, X. Wu, H. Kuang, C. Xu, N. A. Kotov, *Chem. Rev.* **2017**, *117*, 8041.

52 W. Ma, H. Kuang, L. Xu, L. Ding, C. Xu, L. Wang, N. A. Kotov, *Nat. Commun.* **2013**, *4*, 2689.

53 B. Dimitrov, D. Bukharina, D. Nepal, M.E. McConney, T.J. Bunning, V. V. Tsukruk. *Adv. Opt. Mater.*, **2024**, submitted.

54 R. Duan, M. Lu, R. Tang, Y. Guo, D. Zhao, *Biosensors* **2022**, *12*, 707.

55 M. Kim, H. Lee, M. C. Krecker, D. Bukharina, D. Nepal, T. J. Bunning, V. V. Tsukruk, *Adv. Mater.* **2021**, *33*.

56 Y. Kim, B. Yeom, O. Arteaga, S. Jo Yoo, S.-G. Lee, J.-G. Kim, N. A. Kotov, *Nat. Mater.* **2016**, *15*, 461.

57 G. P. J. Jorge, R. Ossikovski, *Polarized light and the Mueller Matrix Approach*; CRC Press: Boca Raton, **2022**.

58 J. N. Hilfiker, N. Hong, S. Schoeche, *Adv. Opt. Technol.* **2022**, *11*, 59.

59 “Ansys Lumerical FDTD simulation of photonic components,” Ansys Inc., 2023, https://www.ansys.com/it-it/products/photonics/fdtd

60 F. M. Zehentbauer, C. Moretto, R. Stephen, T. Thevar, J. R. Gilchrist, D. Pokrajac, K. L. Richard, J. Kiefer, *Spectrochim. Acta A Mol. Biomol. Spectrosc.* **2014**, *121*, 147.

61 C. Zou, D. Qu, H. Jiang, D. Lu, X. Ma, Z. Zhao, Y. Xu, *Molecules* **2019**, *24*, 1008.

62 W. Li, M. Xu, C. Ma, Y. Liu, J. Zhou, Z. Chen, Y. Wang, H. Yu, J. Li, S. Liu, *ACS Appl. Mater. Interfaces.* **2019**, *11*, 23512.

63 M. Xu, Z. Xu, M. A. Soto, Y. Xu, W. Y. Hamad, M. J. MacLachlan, *Adv. Mater.* **2023**, *35*, 2301060.

64 S. Kang, Y. Li, D. Bukharina, M. Kim, H. Lee, M. L. Buxton, M. J. Han, D. Nepal, T. J. Bunning, *Adv. Mater.* **2021**, *33*, 2103329.

65 J. Crassous, M. J. Fuchter, D. E. Freedman, N. A. Kotov, J. Moon, M. C. Beard, S. Feldmann, *Nat. Rev. Mater.* **2023**, *8*, 365.

66 S. Beck-Candanedo, M. Roman, D. G. Gray, *Biomacromolecules* **2005**, *6*, 1048.

67 M. E. McConney, S. Singamaneni, V. V. Tsukruk, *Polymer Reviews* **2010**, *50*, 235.

68 A. Mendoza-Galván, E. Muñoz-Pineda, S. J. Ribeiro, M. V. Santos, K. Järrendahl, H. Arwin, *J. Opt.* **2018**, *20*, 024001.

69 F. S. Richardson, J. P. Riehl, *Chem. Rev.* **1977**, *77*, 773.

70 S. Li, X.-Y. Dong, K.-S. Qi, S.-Q. Zang, T. C. Mak, *J. Am. Chem. Soc.* **2021**, *143*, 20574.